

Current Galactic Chemical Evolution models fail to explain rising Na-abundances of young thick disc stars

Evans K. Owusu^{1,2,3,4}, Ashley J. Ruiter^{1,2,3,4,5}, Alex J. Kemp⁶, Sven Buder^{2,7}, Ivo R. Seitenzahl⁴, Nicolas Rodriguez-Segovia¹, R. Pakmor⁸, Giulia C. Cinquegrana^{2,9}, Nicholas Storm^{3,10}, Philipp Eitner^{3,10}, and Maria Bergemann³

¹*School of Science, University of New South Wales Canberra, Australia Defence Force Academy, ACT 2600, Australia;*

²*ARC Centre of Excellence for All-Sky Astrophysics in 3 Dimensions (ASTRO-3D)*

³*Max-Planck-Institut für Astronomie, Königstuhl 17, D-69117 Heidelberg, Germany;*

⁴*Heidelberger Institut für Theoretische Studien, Schloss-Wolfsbrunnengasse 35, 69118 Heidelberg, Germany;*

⁵*OzGrav: The ARC Centre of Excellence for Gravitational Wave Discovery, Hawthorn, VIC 3122, Australia;*

⁶*Institute of Astronomy (IVS), KU Leuven, Celestijnenlaan 200D, 3001 Leuven, Belgium;*

⁷*Research School of Astronomy and Astrophysics, Australian National University, ACT 2611, Australia;*

⁸*Max Planck Institute for Astrophysics, Karl-Schwarzschild-Str. 1, D-85748 Garching, Germany;*

⁹*School of Physics & Astronomy, Monash University, Clayton, VIC 3800, Australia;*

¹⁰*Heidelberg University, Grabengasse 1, 69117 Heidelberg, Germany;*

Accepted XXX. Received YYY; in original form 2025 June 21

ABSTRACT

We recently identified an upturn in $[\text{Na}/\text{Fe}]$ for the population of Solar-type stars in the Galactic thick disc ($-0.3 < [\text{Fe}/\text{H}] < +0.3$ dex) at super-Solar metallicity in GALactic Archaeology with HERMES (GALAH) data. Here, we investigate the cause of this unexplained Na enrichment between ($[\text{Fe}/\text{H}] \approx 0 - 0.6$ dex) using the OMEGA+ galactic chemical evolution code. We investigate the increase of $[\text{Na}/\text{Fe}]$ with four combinations of nucleosynthetic yields from the literature, with source contributions from core-collapse supernovae, asymptotic giant branch stars, and Type Ia supernovae. We focus on two possible causes for the Na-enhancement: the ‘metallicity effect’ resulting from core-collapse supernovae at super-Solar metallicity and the contribution of metal-rich AGB stars. We adopt two sets of Type Ia supernova yields with one model assuming only Chandrasekhar-mass explosions, and another assuming only sub-Chandrasekhar-mass explosions. We find that the assumed Type Ia explosion has little effect on the $[\text{Na}/\text{Fe}]$ Galactic Chemical Evolution modelling, and all Galactic chemical evolution models tested fail to reproduce the observed $[\text{Na}/\text{Fe}]$ enrichment in the young thick disc population at super-Solar metallicities. Our study indicates a possible ‘under-pollution effect’ by SNe Ia, which are the dominant producers of iron, in the Galactic disc’s Solar-type star population. These findings provide a step forward toward understanding the origin of the unexplained sodium enrichment at super-Solar metallicities in the Galactic disc.

Key words: Galaxy: abundances – Galaxy: evolution – Stars: abundances – Nucleosynthesis

1 INTRODUCTION

Stellar evolution is mainly determined by the initial chemical composition and mass of the star at birth (see e.g., [Appenzeller 1982](#); [Beccari & Carraro 2015](#); [Hayden et al. 2017](#); [Sellwood & Binney 2002](#); [Steinhardt et al. 2023](#)). In turn, the chemical composition of stellar nurseries is influenced by astrophysical processes such as stellar and galactic winds, supernovae (SNe), infalling gas and/or satellite galaxies, and star formation processes ([Gibson et al. 2003](#); [Schoettler & Owen 2024](#)). Consequently, Galactic Chemical Evolution (GCE) studies have been developed to trace the history and evolution of galaxies, as stellar abundances preserve the chemical signature of their birth environment and provide a crucial observational window into their evolution.

All elements heavier than He and Li, from light elements like carbon to heavier ones like barium, are synthesised by one or more

astrophysical channels: For example core-collapse supernovae (CC SNe), which synthesise large amounts of α -elements such as Mg, Si, Ca, Ti; ([Arnett 1978](#); [Nomoto et al. 1997](#); [Kobayashi et al. 2020a,b](#)), Type Ia supernovae (SNe Ia), the dominant source of iron-peak elements such as Cr, Mn, Fe, Co, Ni; e.g., ([Chiappini 2009](#); [Howell 2011](#); [Nomoto et al. 2013](#); [Seitenzahl et al. 2013b](#); [Leung & Nomoto 2017](#); [McWilliam et al. 2018](#); [Bravo et al. 2024](#)), and asymptotic giant branch (AGB) stars, which produce most s-process elements, such as Ba, Sr, Y, and Zr; e.g., ([Karakas & Lattanzio 2007](#); [Cseh et al. 2022](#); [den Hartogh et al. 2023](#)). These three sites are some of the principal astrophysical sources driving GCE and are typically accounted for in GCE models. Additional (and more complex) sources include various types of interacting stars, in many cases undergoing one or more common envelope event(s), such as novae ([Kemp et al. 2024](#)) and kilonovae ([Kobayashi et al. 2023](#); [Matteucci 2023](#)).

Examining the contributions of different astrophysical phenomena toward the chemical enrichment of a galaxy over a wide range of metallicities provides insight into how Galactic processes shape enrichment of elements – such as Na. The analysis of the enrichment pattern helps us trace how each channel influences the build-up of elements (e.g., Na) over time, ultimately shaping its present-day abundance relative to the Solar ratio. An analysis of the logarithmic abundance ratios of elements (X) relative to iron (Fe), expressed as $[X/Fe]^1$, can provide valuable insights into the chemical evolution history of the Galaxy (Francois 1986; Wheeler et al. 1989; Freeman & Bland-Hawthorn 2002; Ratcliffe et al. 2022). Iron is chosen as the reference element because its abundance increases steadily with time in the Universe, and it is relatively straightforward to determine its spectroscopic stellar abundances, particularly compared to elements whose gas-phase abundances are more challenging to measure directly. Furthermore, iron is produced and expelled back into the interstellar medium (ISM) by both CC SNe and SNe Ia (Tsujimoto et al. 1995; Iwamoto et al. 1999; Kobayashi et al. 2006; Recio-Blanco et al. 2014), making it an excellent tracer of overall metallicity and GCE (McWilliam 1997; Jha et al. 2019). This study focuses on Na, which is synthesised during hydrostatic carbon burning in massive stars (i.e., $M_{ZAMS} \geq 8 M_{\odot}$; Woosley & Weaver 1995; Nomoto et al. 2013; Kobayashi et al. 2020b; Arcones & Thielemann 2023). Na is an element with one stable isotope (i.e., monoisotopic), and the next lightest element after Be and F.

In massive stars, during the nucleosynthesis processes, Na is expelled into the ISM before CC SNe through stellar winds, or if kept until the supernova. Factors like stellar mass, mass-loss rates and explosion energies favour Na's explosion (Vink 2018). Further, the amount of Na produced is sensitive to progenitor metallicity (Arnould & Norgaard 1978, i.e., there is a 'metallicity effect'). Na's monoisotopic feature, that is, the isotope ^{23}Na , which produces more neutrons than protons (11p, 12n), makes its nucleosynthetic yields more sensitive to the neutron surplus existing in the progenitor star. Specifically, ^{23}Na production in massive stars during hydrostatic carbon and neon burning depends on the availability of free neutrons, which in turn is set by the initial metallicity of the star (Arnett 1971; Arnould & Norgaard 1978; Arnett 1996; Kobayashi et al. 2006). At higher metallicity (Z), there is a greater abundance of ^{22}Ne – produced from ^{14}N left over from the carbon-nitrogen-oxygen (CNO) cycle. The CNO chain requires these elements as catalysts, meaning that a higher initial Z results in a more efficient hydrogen burning, which then enhances the ^{14}N to ^{22}Ne reaction. ^{22}Ne , being neutron-rich, acts as a reservoir and favours the production of ^{23}Na . Thus, the sensitivity of Na yields to metallicity arises from the specific nucleosynthetic pathway of ^{23}Na and the metallicity-dependent production of ^{22}Ne , rather than it being a general property of all monoisotopic elements. Comparatively, neighbouring even-Z elements like Mg do not possess this property because of their multiple stable isotopes – their yields are less sensitive to the neutron excess (and hence progenitor metallicity) as production can shift from e.g. ^{24}Mg to ^{25}Mg or ^{26}Mg when metallicity changes. This dependence on progenitor metallicity allows Na to serve as an effective tracer of Galactic chemical evolution. In contrast, at lower metallicity, the initial abundances of CNO elements are reduced, leading to less ^{14}N and consequently less ^{22}Ne and neutron excess. This results in lower yields of ^{23}Na (Timmes et al. 1995; Kobayashi et al. 2020a).

Similarly, intermediate-mass–mass stars on the AGB play a significant role in Na synthesis, with their contribution strongly dependent

on metallicity. At high metallicity, the second dredge-up efficiently mixes CNO – processed material, particularly ^{14}N , to the stellar surface early in the AGB phase. This process leads to increased secondary production of both nitrogen and Na as metallicity rises, and remains robust across a range of metallicities (Ventura et al. 2013; Karakas & Lattanzio 2014; Cristallo et al. 2015). In contrast, Na production is dominated by hot bottom burning (HBB) at lower metallicity. Here, the third dredge-up brings freshly synthesised carbon into the envelope, which is converted to Na via the Ne-Na cycle during HBB. Because HBB operates at higher temperatures in metal-poor stars, this pathway enables efficient primary ^{23}Na production even when the initial metal content is low. Recent AGB models by Cinquegrana & Karakas (2022) confirm these trends: They show that ^{23}Na yields increase with metallicity due to secondary production at high Z, while primary production via HBB remains significant at low Z (see their fig. 4). The usefulness of Na in the context of the 'metallicity effect' has been discussed before; for a detailed discussion of the metallicity effect associated with Na abundance, see Arnould & Norgaard (1978); Shi et al. (2004) and section 4.1 of (Owusu et al. 2024, hereafter O24).

Historically, Cayrel de Strobel et al. (1970) first reported evidence of Na enrichment in dwarf and giant stars. Subsequent studies (e.g., Francois 1986; Matteucci & Greggio 1986; Edvardsson et al. 1993; Mowlavi 1999; Shi et al. 2004) have confirmed a Na upturn and enrichment with increasing metallicity across various stellar populations (halo, bulge and disc). Cayrel de Strobel et al. (1970) laid the essential groundwork for understanding Na production in massive stars. Later on, Francois (1986) underscored the critical role AGB star progenitors play in Na enrichment, thereby expanding our understanding of Na's nucleosynthetic contribution across different stellar populations. Additionally, Takeda & Takada-Hidai (1994) found that A – F supergiant stars exhibit an excess in Na with $[Na/H]$ having values ranging from $0.0 \leq [Na/H] \leq 0.5$ in F supergiants and $0.7 \leq [Na/H] \leq 0.8$ in A supergiants. This enhancement is credited to the Ne-Na cycle during hydrogen burning. More recent high-resolution spectroscopic surveys have demonstrated that this trend is particularly pronounced at super-Solar metallicities ($[Fe/H] > 0$), where $[Na/Fe]$ shows a clear increase in both old and young Milky Way disc stars (O24). The Na enrichment at super Solar $[Fe/H]$ is especially notable in the metal-rich, dynamically cold younger-thick disc population, a trend that has been reported in other studies (Bensby et al. 2014, 2017; Nissen et al. 2020; Griffith et al. 2022). In particular, Bensby et al. (2014) documented an increase in $[Na/Fe]$ with $[Fe/H] > 0$ for a sample of 714 dwarf stars in the Solar neighbourhood (see their fig. 16). Despite these reports of an upturn in Na enrichment at high metallicity, a universally accepted explanation remains elusive. These differing interpretations for the observed increase in Na, as well as contributions from different nucleosynthesis channels, motivated us to study the observed progressive rise in $[Na/Fe]$ at high metallicity. It presents important implications for understanding nucleosynthesis sources and GCE.

This paper is organised into five sections. In Section 2, we describe the data and the processing of yield tables for the various theoretical stellar yields employed in this study. Additionally, we outline the choice of GCE code used. Section 3 presents the results of this work, while Section 4 discusses these results and their implications for broader nucleosynthesis processes. Finally, Section 5 concludes with a summary of our findings and highlights opportunities for future research.

¹ $[X/Fe] \equiv \log_{10}(N_X/N_{Fe})_{\star} - \log_{10}(N_X/N_{Fe})_{\odot}$

2 CHEMICAL EVOLUTION DATA AND MODELLING METHODOLOGY

In the third data release of the GALactic Archaeology with HERMES spectrograph (GALAH DR3, [Buder et al. 2021](#)), Na is one of the 30 elemental abundances analysed. The dataset includes Na lines at $\lambda 4751.82\text{\AA}$, $\lambda 5682.63\text{\AA}$ and $\lambda 5688.21\text{\AA}$, with abundances derived using one-dimensional, non-local thermodynamic equilibrium (1D NLTE) modelling ([Amarsi et al. 2020](#)). In Figure 1, we show the GALAH DR3 [Na/Fe] abundances for a sample of 5 148 Solar-type stars (thick disc only), similar to what was discussed in O24, but with a higher metallicity range in the sample up to +0.6 dex to incorporate an extended population in metallicity-space. The reason for the observed [Na/Fe] upturn in the GALAH data is currently unknown and is the focus of this paper. This work aims to investigate the underlying cause of Na abundance enrichment at super-Solar metallicities (up to 0.6 dex) among the younger population of the old (thick) disc stars of the Galaxy.

We create four GCE models (see Table 1) that incorporate different stellar yield predictions from theoretical nucleosynthesis calculations of CC SNe, SNe Ia, and AGB stars and compare these with observational data. We explore two possibilities for the Na enhancement: the ‘metallicity effect’ from CC SNe at high metallicity and AGB stars at super-Solar metallicity, as possible solutions for explaining the observed Na enhancement. Firstly, the metallicity effect from CC SNe motivated us to examine normalised Na production ratios using data from [Woosley & Weaver \(1995\)](#). A preliminary check into those models (see Figure 2) seemed to support the idea that the metallicity effect plays an important role in Na production. We therefore expand our yield table sets (see Table 1) to include massive star yields from [Woosley & Weaver \(1995\)](#) in addition to existing massive star yield tables in OMEGA+ (i.e., [Kobayashi et al. 2006](#); [Limongi & Chieffi 2018](#)). Secondly, we include [Cinquegrana & Karakas \(2022\)](#) mass- and metallicity-dependent AGB yields, which cover a broad range of super-solar metallicities ($0.04 \leq Z \leq 0.1$), into our chemical evolution models (see Section 2.2.2 and Table 1 for model K10C22K06). The super-Solar metallicity AGB models clearly show an increasing ^{23}Na yield with increasing metallicity (see their fig. 8). By incorporating both of these additional yield sets, we account for Na enrichment from both CC SNe and AGB channels.

2.1 Sample selection

Similar to O24, we selected a sample of Solar-type (G spectral type) thick disc stars from the GALAH DR3 catalogue with quality cuts based on the following criteria:

$$\begin{aligned} \text{flag_sp} &== 0, \text{flag_fe_h} == 0, \text{flag_Na_fe} == 0, & (1) \\ \text{e_age_bstep}/\text{age_bstep} &< 0.2 \text{ or } \text{e_age_bstep} < 2, & (2) \\ \text{snr_c2_iraf} &> 50, & (3) \\ 5600 &< T_{\text{eff}} < 5950, \log g > 4.15, & (4) \\ -0.3 &< [\text{Fe}/\text{H}] < +0.6. & (5) \end{aligned}$$

Equation 1 describes the basic quality criteria applied to our sample. Equation 2 selects stars with a reliable age estimate, specifically those with uncertainties below 20% or less than 2 Gyr. Equation 3 ensures high-quality spectra by requiring a signal-to-noise ratio greater than 50 per pixel in the green CCD ([Kos et al. 2017](#)). Finally, in Equation 4 and 5, we place additional constraints to select only Solar-type stars. In addition, we also apply the standard O24 selection criterion for thick disc stars only. Old stars : $[\text{Na}/\text{Fe}]_{\text{old}} > 0.55 - (0.5/5.5) \times \tau$; where τ is the stellar age in Gyr. However, compared to O24, we

extended the metallicity range beyond $[\text{Fe}/\text{H}] = +0.3$ to capture a broader abundance distribution (see Equation 5). This wider range enables us to gain insights into Na enhancement trends. Following these criteria, our final sample consists of 5 148 Solar-type thick disc stars, as illustrated in Figure 1, which displays the resultant sample on a $[\text{Fe}/\text{H}]$ vs $[\text{Na}/\text{Fe}]$ plane. Significantly, we observe a persistent rising trend commencing at $[\text{Fe}/\text{H}] > 0$.

2.2 Chemical evolution with OMEGA+

We used the two-zone GCE code OMEGA+² ([Côté et al. 2018](#)), an extended version of the One-zone Model for the Evolution of Galaxies ([Côté et al. 2017](#); [Côté & Ritter 2018](#), OMEGA). OMEGA+ simulates a central, cold, star-forming region surrounded by a hot gas reservoir, enabling detailed modelling of Galactic processes, their timescales, and the formation history of the Galaxy ([Côté et al. 2018](#)). The two-zone structure of OMEGA+ consists of a galaxy and a circumgalactic medium (CGM), which offers the following advantages:

- Self-consistent star formation rate (SFR): OMEGA+ computes the SFR by balancing galactic inflows against stellar feedback without requiring external input.
- Recycling of metals: Metals ejected from the central galaxy are retained within the CGM rather than lost. These metals can later be reintroduced to the star-forming region via galactic inflows, allowing for a more realistic simulation of the Galaxy’s chemical evolution.
- Key parameters of the model include the initial mass function (IMF), adopted from the prescription of [Kroupa \(2001\)](#), the star formation rate (SFR), (calculated using the Kennicutt–Schmidt law, [Kennicutt 1998](#)), gas flows (inflow/outflow) and the initial mass of gas (mgal).

While our observational data only represent a sub-component of the Galaxy’s thick disc and not the entire Galaxy, the goal of the study is to determine if the observed Na-enhancement at super-Solar metallicity is, to first order, able to be reproduced with a GCE code. OMEGA+ shares similarities with other GCE codes, such as the Versatile Integrator for Chemical Evolution (VICE, [Johnson et al. 2021](#)), the flexible one-zone chemical evolution code (FlexCE, [Andrews et al. 2017](#)), the Bayesian chemical evolution code ChemPy ([Rybicki et al. 2017](#)), and the Galactic Evolution tool (GETool, [Fenner et al. 2002](#)). In OMEGA+, gas flows are treated with two key assumptions. First, we assume that inflows are predominantly primordial in composition. Second, we model outflows as metal-enriched, allowing their metallicity to vary over time. These assumptions directly impact the predicted chemical evolution of the stimulated galaxy, shaping the enrichment history and the metallicity distribution of stars. OMEGA+ can better reproduce observed features such as the metallicity distribution function (MDF) and abundance patterns in stellar populations ([Côté et al. 2016](#)) by allowing the metal loading of outflows to change with time. In contrast, assuming constant metal loading or ignoring enriched outflows would result in significant discrepancies between the model predictions and observed chemical signatures. Table 2 outlines our adjusted physical parameters. The GCE model was evolved for 13 Gyr.

Type Ia supernovae (SNe Ia) are crucial in GCE models as they dominate the production of iron-peak elements (e.g., Fe, Mn, Ni), contributing $\sim 70\%$ of the Milky Way’s iron inventory ([Matteucci et al. 2009](#); [Fink et al. 2012](#); [Bovy 2015](#); [Maoz et al. 2018](#); [Jha](#)

² Publicly available at <https://github.com/becot85/JINAPyCEE>

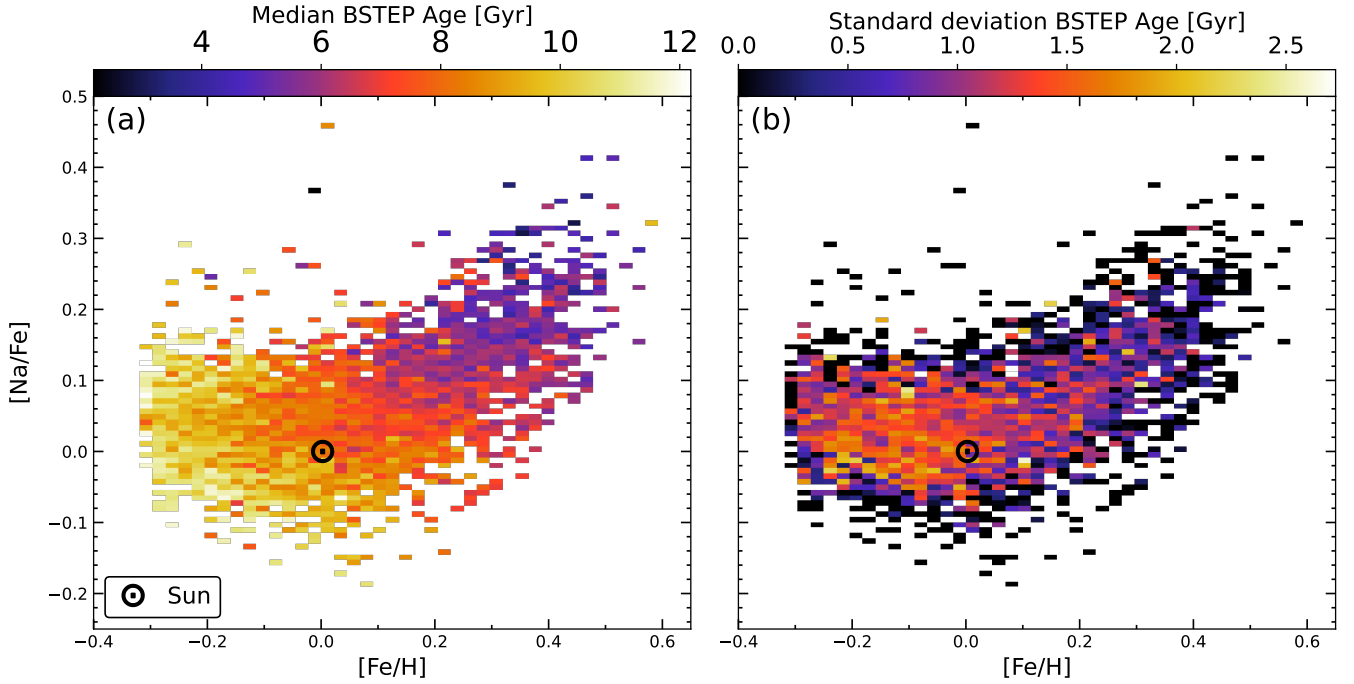


Figure 1. $[\text{Na}/\text{Fe}]$ as a function of metallicity $[\text{Fe}/\text{H}]$ for the sample of Solar-type stars from GALAH DR3 used in this work (see Section 2). The left panel (a) shows the distribution coloured by stellar age, illustrating the median stellar age (in Gyr) at each $([\text{Fe}/\text{H}], [\text{Na}/\text{Fe}])$ bin. The right panel displays the same distribution, highlighting the standard deviation in stellar age within the corresponding bins. The Bayesian Stellar Parameters Estimator (BSTEP) was used to compute the stellar ages. The Solar abundance position is marked by the symbol (\odot) at $[\text{Fe}/\text{H}], [\text{Na}/\text{Fe}] = (0, 0)$.

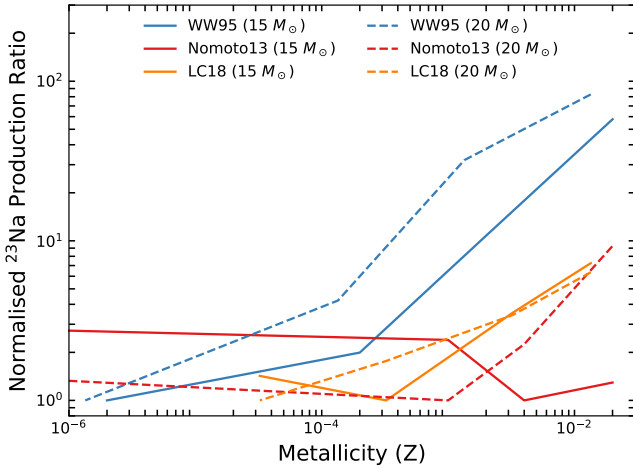


Figure 2. Normalised Na (^{23}Na) production ratios as a function of stellar metallicity (Z) for massive stars with initial masses 15 and 20 M_{\odot} . The models shown are massive star yields from [Woosley & Weaver \(1995, WW95, blue triangles\)](#), [Nomoto et al. \(2013, Nomoto13, red circles\)](#) and [Limongi & Chieffi \(2018, LC18, orange squares\)](#). The normalised production ratio (y-axis: Normalised ^{23}Na Production Ratio) is calculated for each model by dividing the raw ^{23}Na yield at each metallicity by the minimum ^{23}Na obtained across all metallicities for that specific model. This normalisation highlights the relative change in Na production as a function of metallicity for each set of stellar models.

[et al. 2019](#)). Unlike CC SNe, which primarily enrich the ISM with α -elements such as O and Mg on short timescales (~ 10 Myr), SNe Ia inject iron with a delay time spanning ~ 50 Myr to a Hubble time. This delay creates the observed downturn in $[\alpha/\text{Fe}]$ ratios as

Table 1. Yield tables used and the resulting models. The ‘model’ reflects the combined selections of AGB and massive stars in each nucleosynthesis yield table (see Section 2.2.2 for details of each model). Chandrasekhar-mass (M_{Ch}) Type Ia supernovae yields are adopted from S13 and sub-Chandrasekhar-mass (sub- M_{Ch}) Type Ia supernova yields are adopted from P22. Models are explained in the footnote.

AGB	Massive star	SN Ia	Model
K10	LC18	S13/P22	K10LC18
K10	WW95	S13/P22	K10WW95
K10	K06	S13/P22	K10K06
K10, C22	K06	S13/P22	K10C22K06

¹ LC18: [Limongi & Chieffi \(2018\)](#); WW95: [Woosley & Weaver \(1995\)](#); K06: [Kobayashi et al. \(2006\)](#); K10: [Karakas \(2010\)](#); C22: [Cinquegrana & Karakas \(2022\)](#); S13: [Seitenzahl et al. \(2013a\)](#) and P22: [Pakmor et al. \(2022\)](#).

$[\text{Fe}/\text{H}] > -1$ in stellar populations, distinguishing chemically distinct Galactic components (e.g., thick vs. thin disc, [Matteucci et al. 2009](#); [Dubay et al. 2024](#); [Cavichia et al. 2024](#)). SNe Ia also produce more iron per event than CC SNe, making them indispensable for reproducing the G-dwarf metallicity distribution and explaining Solar abundance patterns ([Kobayashi et al. 2020a](#)). To first order, SNe Ia can be split into two categories when considering their nuclear yields: Chandrasekhar- and sub-Chandrasekhar-mass explosions. Given that both categories of SNe produce distinct elemental yields in varying amounts and often with different injection timescales, and given the ongoing uncertainty surrounding the nature of SN Ia progenitors, we incorporate yields from one of each broad category into our GCE models. Though it is widely agreed that various formation channels

Table 2. Default and adjusted stellar parameters used in this work for the OMEGA+ GCE model. The star formation efficiency is a dimensionless scaling quantity and a free parameter (see Equations 13 and 14 of Côté et al. 2018)

Stellar parameters	Default values	Adjusted values
Initial mass function (IMF)	1 – 30 M_{\odot}	1 – 130 M_{\odot}
Star formation efficiency (SFE; ϵ_{\star})	3.0×10^{-9}	3.0×10^{-10}
Initial mass of gas in simulation (mgal)	$1.0 \times 10^{10} M_{\odot}$	$2.0 \times 10^{11} M_{\odot}$

of Type Ia supernovae are predicted to have different delay time distributions (DTD, see Ruiter et al. 2011; Eitner et al. 2023), as a first step, we adopt the DTD from Maoz et al. (2012), which is the default implementation in OMEGA+.

For simplicity, we assume either Chandrasekhar-mass delayed detonations or sub-Chandrasekhar-mass prompt detonations in white dwarf mergers, and apply the Maoz et al. (2012) DTD for both cases. For the Chandrasekhar mass explosions, we use the N100 model yields from Seitzzahl et al. (2013a) for 4 metallicities ($Z = 0.0002, 0.002, 0.01$ and 0.02). For the sub-Chandrasekhar mass explosions, we use yields from the two-explosion double white dwarf merger model of Pakmor et al. (2022), currently one of the most favoured scenarios for SNe Ia (see Ruiter & Seitzzahl 2025, for a recent review). Since only Solar metallicity yields are available for the merger model, we adopt these for the entire metallicity range sampled in our GCE study when the sub-Chandrasekhar mass scenario is assumed.

2.2.1 Parameters for the GCE code

Table 2 presents both default and adjusted stellar parameters used in OMEGA+ for this study. The default settings of OMEGA+ produce $[\text{Fe}/\text{H}]$ values only up to approximately 0.2 dex. To model higher metallicities, we modified these default parameters (see Section 3.1), allowing the machinery to reach $[\text{Fe}/\text{H}]$ values at higher super-Solar metallicities (i.e., $[\text{Fe}/\text{H}] \sim 0.6$ dex), which overlaps the AGB star yields in one of our models (see K10C22K06 in Table 1), enabling the models to overlap with the observations. In addition, the upper bound of the initial mass function (IMF) is increased to allow sampling from the high mass ($M = 120 M_{\odot}$) model of LC18. These updated parameters allow the OMEGA+ code to reach a metallicity of $[\text{Fe}/\text{H}] \sim 0.6$ dex, ensuring our GCE models encompass the full metallicity range observed in the thick disc sample.

2.2.2 Stellar Nucleosynthesis Yields

For all GCE simulations, nucleosynthetic yields constitute an integral ingredient. The yields consist of materials expelled by each isotope from the different nucleosynthesis channels. The nucleosynthesis yields adopted in our GCE models represent the total mass of chemical species expelled by a star over its lifetime. These yields are computed following the methodology presented in Karakas & Lattanzio (2007), using the equation:

$$M_i = \int_0^{\tau} [X(i) - X_0(i)] \frac{dM}{dt} dt, \quad (6)$$

where M_i denotes the yield of a given species, $\frac{dM}{dt}$ is the stellar mass loss rate at time t , $X(i)$ and $X_0(i)$ are the current and total mass fractions of the species, respectively, and τ is the total lifetime of

the stellar model. A positive yield indicates the net production of the species during the star’s evolution, whereas a negative yield signifies destruction relative to the star’s initial abundance.

Our study incorporates several yield datasets covering various stellar masses and metallicities. For low- to intermediate-mass stars (AGB stars) with metallicities up to Solar ($Z_{\odot} = 0.02$, Lodders et al. 2009), we adopt yields from Karakas (2010, hereafter K10), covering masses between 1.0 and 6.0 M_{\odot} and metallicities at Solar and below-Solar (i.e., $Z = 0.0001, 0.008, 0.004$ and 0.02). Additionally, new high-metallicity (Z) AGB yields from Cinquegrana & Karakas (2022, hereafter C22) have been included, spanning metallicities in the range $0.04 \leq Z \leq 0.1$ and stellar masses from 1.0 to 8.0 M_{\odot} in increments of 0.5 M_{\odot} . Using the relation $[\text{Fe}/\text{H}] \approx \log_{10} \left(\frac{Z}{Z_{\odot}} \right)$, the metallicity range from C22 corresponds approximately to $0.3 \leq [\text{Fe}/\text{H}] \leq 0.7$.

For massive stellar yields (from CC SNe), we use yield data from three different studies: Woosley & Weaver (1995, hereafter WW95), Kobayashi et al. (2006, hereafter K06), and Limongi & Chieffi (2018, hereafter LC18). Each CC SN model listed in Table 1 adopts a distinct explosion mechanism, significantly influencing GCE predictions. Specifically, the K06 model assumes a piston-driven explosion with a fixed explosion energy, typically around 1.2×10^{51} erg. The WW95 model employs the KEPLER hydrodynamic code, also using a piston-driven mechanism, but explores a wider range of explosion energies ($0.3 - 3.0 \times 10^{51}$ erg) without including mixing processes. Finally, the LC18 model utilises hydrodynamic simulations with a kinetic bomb mechanism, incorporating variable explosion energies, variable remnant mass cuts, and feedback effects. The WW95 yields, which specifically cover stellar masses of 13, 15, 18, 20, 25, 30, and 40 Solar masses, have been included because our preliminary results from Figure 2 suggest that these yields produce enhanced Na abundances at higher metallicities. We observe that the mass range for WW95 is capped at 40 solar masses, in contrast to the IMF adjusted value of 130 Solar masses. This discrepancy will likely lead to potential underrepresentation of Na nucleosynthesis contributions from CC SNe from very high-mass stars.

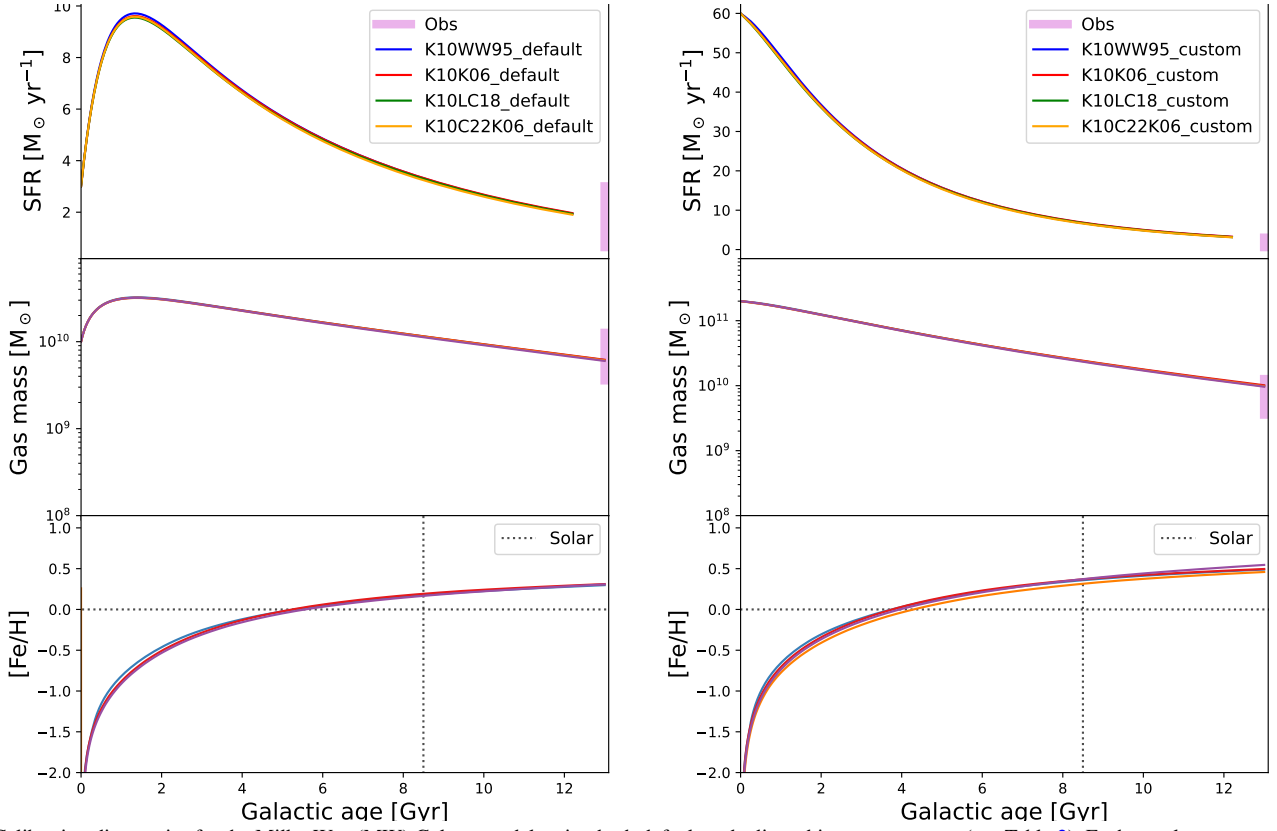
Lastly, for Type Ia supernovae (SNe Ia), we use yields from (Pakmor et al. 2022, P22), computed at Solar metallicity ($Z = 0.02$) based on their ‘two-explosion’ model of two merging white dwarfs and (Seitzzahl et al. 2013a, S13) Chandrasekhar-mass explosion. Although the choice between the single and double explosion models has minimal impact on the overall GCE results (see Figure A1), we consistently apply either the S13 Chandrasekhar-mass or the P22 sub-Chandrasekhar-mass explosion model in our simulations. Table 1 summarises the adjusted values used for the GCE prediction for each model label in this study, and Table 3 lists the raw Na and iron yield for the different categories of SNe Ia and CC SNe used in this study.

3 RESULTS

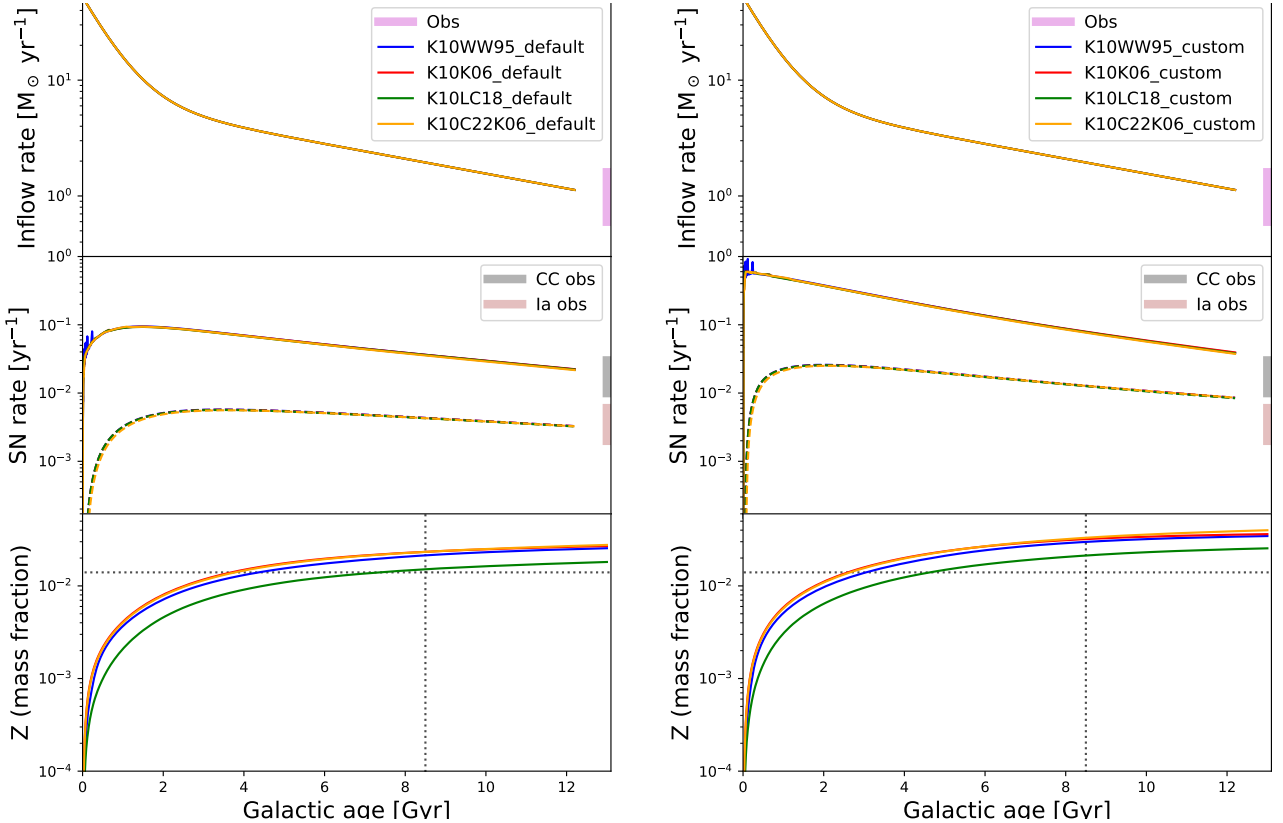
In this Section, we compare the GALAH DR3 observational data for thick-disc Solar-type stars with our GCE model predictions obtained using OMEGA+ and adjusted stellar yields. In short, we find that none of our GCE models reproduce the upturn in $[\text{Na}/\text{Fe}]$, with this ratio instead declining for $[\text{Fe}/\text{H}] > 0$.

3.1 Milky Way model comparison

Figure 3 (i.e., 3a and 3b) illustrates the Galactic properties used to validate our baseline Milky Way model, based on the values in Table



(a) Calibration diagnostics for the Milky Way (MW) Galaxy model, using both default and adjusted input parameters (see Table 2). Each panel presents model predictions for specific Galactic parameters, with vertical shaded bands (pink) representing observational constraints from [Kubryk et al. \(2015\)](#). For calibration purposes only, the Chandrasekhar-mass Type Ia supernovae of [Seitenzahl et al. \(2013a\)](#) were adopted for both default and adjusted models.



(b) Comparison between default and adjusted calibration of the MW using parameters from Table 2. Model labels follow those defined in Table 1 across various diagnostic parameters.

Figure 3. Bulk galactic properties of our model Galaxy based on adjusted model parameters.

Table 3. Yields in M_{\odot} of Na-23 and Fe-56 isotopes for CC SNe and the two Type Ia supernova explosion models used in this work: Chandrasekhar-mass (MCh) model from S13 and sub-Chandrasekhar-mass (sub-MCh) model from P22 (see Table 1). **Note:** Solar metallicity yields are shown, although yield values for additional metallicities are included from S13 in our GCE modelling (i.e., $Z = 0.0002$, 0.002 , and 0.01). The integrated yield per solar mass for different massive star yields used in this work has been computed and normalised using the [Salpeter \(1955\)](#) IMF ($\alpha = 2.35$, at $Z = 0.02$).

Model	Mass Range (M_{\odot})	^{23}Na (M_{\odot} per event)	^{56}Fe (M_{\odot} per event)
WW995	11–40	8.454×10^{-5}	1.941×10^{-3}
K06	13–40	1.049×10^{-4}	1.742×10^{-3}
LC18	13–120	8.406×10^{-5}	1.603×10^{-3}
SN Ia (MCh)	—	3.74×10^{-5}	6.22×10^{-1}
SN Ia (sub-MCh)	—	1.99×10^{-4}	4.87×10^{-1}

2. The outcome as a result of the adjustment in SFE and `mga1` resulted in higher SFR as seen in Figure 3a – with the adjusted parameters having a higher SFR at earlier epochs ($\approx 60 M_{\odot} \text{ yr}^{-1}$) compared to the default parameters ($\approx 9 M_{\odot} \text{ yr}^{-1}$). The increase in star formation creates greater metal production, which contributes to greater [Fe/H] values over time. The substantial initial gas mass promotes vigorous early star formation, accelerating chemical enrichment ([Krumholz & Dekel 2012](#)). The elevated SFRs from the adjusted initial gas conditions align with the equilibrium frameworks of [Krumholz & Dekel \(2012\)](#), showing that excess gas accretion can temporarily boost SFRs until equilibrium is reached ([Tinsley & Larson 1978](#)).

The adjusted configuration shows higher [Fe/H] as a function of stellar age, reflecting a universal relationship between metallicity and the stellar-to-gas mass ratio. [Zahid et al. \(2014\)](#) demonstrated that higher initial gas masses accelerated metal production, directly raising [Fe/H] over time. This supports the concept of ‘gas processing equilibrium,’ where metal yields are governed by the balance between gas accretion and star formation ([Tinsley & Larson 1978](#); [Köppen & Edmunds 1999](#)). Consequently, it is expected that the adjusted parameters produce higher metallicity environments at ‘modern’ galaxy ages. In the upper panels of Figure 3b, the inflow rates for both default and adjusted models remained unchanged. The inflow rates span roughly $1 - 10 M_{\odot}/\text{yr}$, reflecting standard assumptions regarding gas accretion from the circumgalactic medium for Milky Way-like galaxies ([Sánchez Almeida et al. 2014](#)). For SNe rates as a function of Galactic age, the CC SNe rates display pronounced initial peaks at early Galactic ages (around $1 - 4$ Gyr) in both default and adjusted models, with the adjusted model displaying enhanced rates, a consequence of the larger mass and SFR. In addition, all models (default and adjusted) agree reasonably well with the observational data at ~ 13 Gyr. Finally, the metallicity evolution (i.e., mass fraction, Z) as a function of age for all models demonstrated the expected monotonic increase in Z . The default parameters achieve modest metallicity enrichment, rising gradually.

3.2 Abundance, age, metallicity plane

Here, we describe the different results based on Figure 4. In all panels, the data are those described in Section 2.

- **[Fe/H] vs Age (panel a):** All models show a general trend of increasing [Fe/H] with decreasing stellar age. In particular, the K10C22K06 and K10K06 models closely follow each other, reaching higher [Fe/H] values at younger ages compared to the K10LC18 and K10WW95 models. This hints at CC SNe being the key ingredient in these simulations. The observational data show a spread in [Fe/H] across all ages, with a slight trend of higher [Fe/H] at younger ages. The observed trend (spread) in the observational data is corroborated

with the age metallicity relation (AMR) previously reported in other works (e.g., [Sellwood & Binney 2002](#)).

- **Age vs. [Fe/H] (panel b):** This panel presents the same information as panel (a) but with axes swapped. The data indicate a large scatter in [Fe/H] for stars of similar age.

- **[Fe/H] vs [Na/Fe] (panel c):** All models exhibit an initial increase in [Na/Fe] as [Fe/H] increases, followed by a general decline beyond solar metallicity, with the decrease occurring at different [Fe/H] values for each model. The K10WW95 model best matches the [Na/Fe] and [Fe/H] parameter space, but it does not display the observed enrichment trend at [Fe/H] > 0 .

- **Age vs [Na/Fe] (panel d):** Depending on the model, there is a general trend of decreasing [Na/Fe] with stellar ages older than around 9 Gyr or so. The K10C22K06 model predicts higher [Na/Fe] values for younger stars compared to other models. The observational data show a flat trend in older stars until around 6.5 Gyr, after which there is a slight increase in [Na/Fe] in younger stars. The increasing [Na/Fe] with decreasing stellar age is less obvious in these data than in the [Na/Fe] vs. metallicity parameter space (panel c).

- **[Fe/H] vs [Na/H] (panel e):** Both models and observational data display a continued rise in the [Na/H] vs. [Fe/H] plane. The two models with CC SNe from K06 have a higher [Na/H] than the other two models with different CC SNe yields. For instance, the model with CC SNe from LC18 lies below the data, while WW95 more closely matches the data.

- **Age vs [Na/H] (panel f):** Models predict decreasing [Na/H] with increasing stellar age. The K10C22K06 and K10K06 models show higher [Na/H] values for younger stars compared to K10LC18 and K10WW95. Also, observational data show a weak trend of decreasing [Na/H] with age, with considerable scatter.

We note that the contribution of sub-MCh SNe Ia from [Pakmor et al. \(2022\)](#) resulted in higher [Na/Fe] abundances across all models for the various age, metallicity and [Na/Fe] planes explored as shown in Figure 4. In this sub-Chandrasekhar mass model, Na yields from SNe Ia are 5 times higher than in the Chandrasekhar mass model of [Seitenzahl et al. \(2013a\)](#), while iron production is ~ 22 per cent lower.

4 DISCUSSION

The adjustment to the IMF in Table 2 affects how much Na is produced in the Galaxy, mainly because of the different amounts produced by CC SNe and SNe Ia. Specifically, CC SNe contribute on average $\sim 10^{-5} - 10^{-4} M_{\odot}$ per event, while some SN Ia make on average $2 \times 10^{-4} M_{\odot}$ Na per event. From Table 3, CC SN yields are typically lower, ranging from ~ 0.8 to $1 \times 10^{-4} M_{\odot}$ per event. On the other hand, SNe Ia exhibit more varied yields, with MCh explosions releasing about $3.74 \times 10^{-5} M_{\odot}$ per event and sub-MCh explosions producing significantly more, around $1.99 \times 10^{-4} M_{\odot}$ per event. Although individual sub-MCh SNe Ia can release comparable or even greater amounts of Na than single CC SNe (see GCE line predictions in Figure 4) per event, their overall Galactic contribution remains comparatively small due to their lower occurrence rates relative to CC SNe ([Li et al. 2011](#)). This frequency disparity ensures that, cumulatively, CC SNe dominate Na enrichment in the Galaxy, despite their lower per-event yields. However, because SNe Ia are primary contributors of iron (Fe), their metallicity-dependent yields, currently modelled predominantly at Solar metallicity, could disproportionately influence [Na/Fe] ratios at [Fe/H] > 0 .

Even though our current models can show the overall pattern in [Na/Fe] for values between about -0.4 and 0 , none of the models

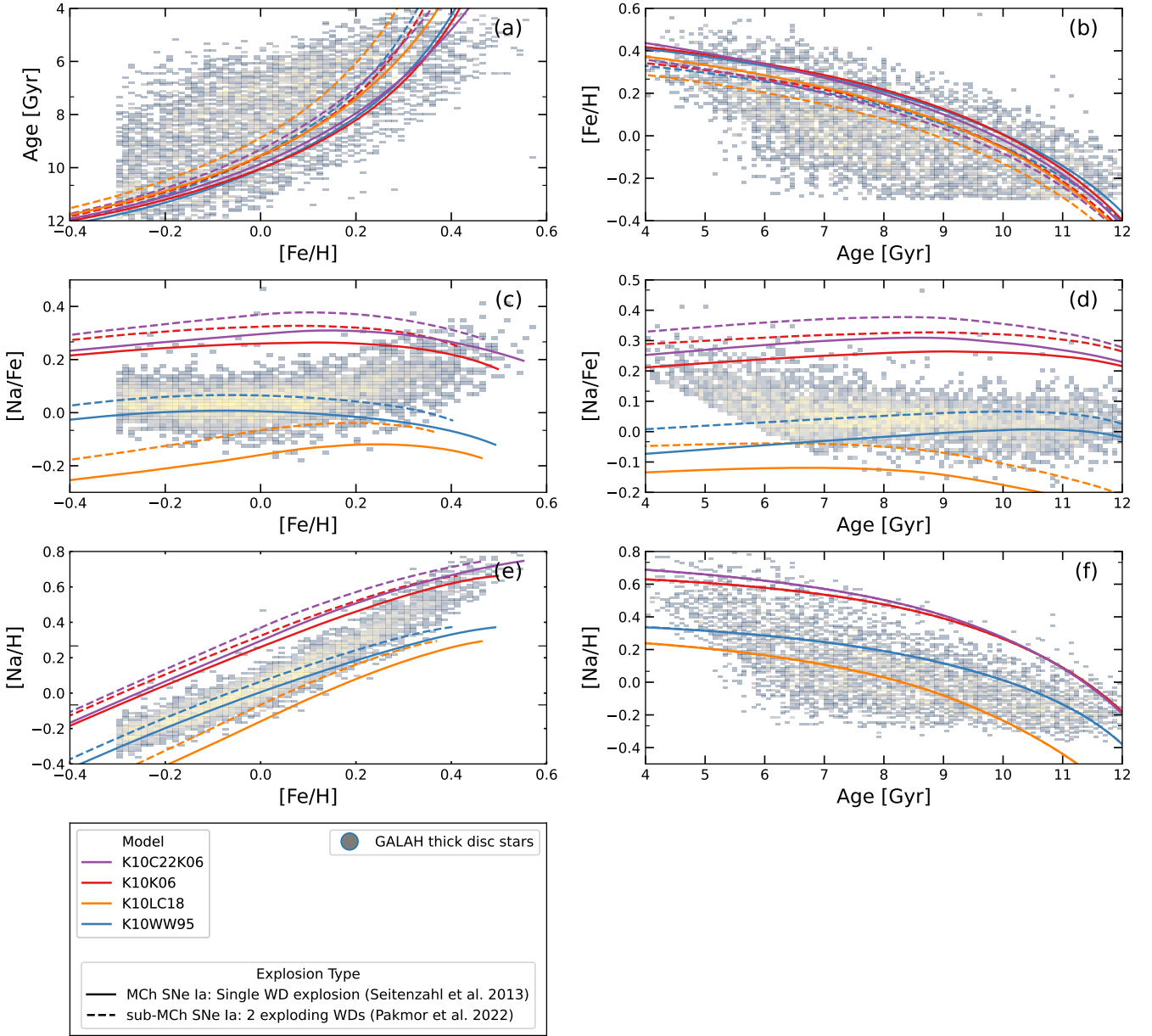


Figure 4. Panels (a)–(f) are the $[\text{Fe}/\text{H}]$ -age, age- $[\text{Fe}/\text{H}]$, $[\text{Fe}/\text{H}]$ - $[\text{Na}/\text{Fe}]$, age- $[\text{Na}/\text{Fe}]$, $[\text{Fe}/\text{H}]$ - $[\text{Na}/\text{H}]$ and age- $[\text{Na}/\text{H}]$ planes, produced by our adjusted GCE code parameters for this study. ‘Age’ here refers to stellar ages. The grey bins are Solar-age thick disc stars selected from the GALAH DR3 catalogue using Equation 5, with the yellow area having a higher concentration of stars. Solid lines represent GCE models in which all SN Ia explosions are assumed to be from Chandrasekhar mass WDs, while for the dashed lines, sub-Chandrasekhar mass explosions from WD mergers are assumed. We defined the model label in Table 1. SN Ia contribution is based on the two-exploding white dwarf from (Pakmor et al. 2022) and delayed detonation for Chandrasekhar-mass white dwarfs, as described in (Seitenzahl et al. 2013a).

can explain the increase in $[\text{Na}/\text{Fe}]$ that we see in the data (Figure 4c). Although both K10K06 and K10C22K06 models share the same CC SNe yield tables, the K10C22K06 model includes additional yields from AGB stars with higher metallicity. Hence, as expected, both models behave similarly, with the K10C22K06 scaling higher $[\text{Na}/\text{Fe}]$ as a function of $[\text{Fe}/\text{H}]$ compared to the other models. Both of these models predict significantly higher $[\text{Na}/\text{Fe}]$ across the whole metallicity range explored, while the K10LC18 model predicts sub-Solar $[\text{Na}/\text{Fe}]$ values throughout. We note, however, that the K10LC10 model shows a promising upturn in $[\text{Na}/\text{Fe}]$, though its

value begins to flatten out and then decrease at around $[\text{Fe}/\text{H}] \sim 0.2$ dex.

The K10WW95 model matches the observed trend of $[\text{Na}/\text{Fe}]$ correctly in the lower metallicity range, but it shows a decrease in $[\text{Na}/\text{Fe}]$ at higher metallicities compared to what we see in the data. A previous study by Eitner et al. (2020) examining manganese abundances ($[\text{Mn}/\text{Fe}]$ vs. $[\text{Fe}/\text{H}]$; see their fig. 2) highlighted differences in the explosion mechanisms of core-collapse supernovae as a likely explanation for the discrepancies between their NLTE data (i.e., 42 stars including red giants and FG dwarf stars taken from different studies) and model predictions. Similarly, we attribute differences

in our GCE model behaviour to the different CC explosion mechanisms used in Woosley & Weaver (1995); Kobayashi et al. (2006) and Limongi & Chieffi (2018).

Prior work using massive star yields by Kobayashi et al. (2011, 2020b) indicated a plateau around Solar metallicity with a slight bump increase at sub-Solar metallicities. In a similar study of G-dwarf stars, Matteucci (2014) used massive star yields from Woosley & Weaver (1995) but also looked at low- and intermediate-mass stellar yields from van den Hoek & Groenewegen (1997) for values between -3.5 and 0.2 in $[\text{Fe}/\text{H}]$. This resulted in a GCE prediction that appeared rather flat at Solar metallicity (see their fig. 2.22). Comparing their result to our findings, our GCE prediction flattens briefly at Solar metallicities and then decreases. This difference is probably due to the different amounts of elements produced, the ways stars explode, how AGB stars are considered, and the different assumptions made in the GCE codes used in each study. In addition, we note that:

- Our observational sample represents only a portion of the Galaxy’s stellar disc population and does not fully capture the diversity of chemical evolution across the entire Galaxy. Note that our GCE modelling uses OMEGA+, which is calibrated to the Milky Way Galaxy as a whole.
- The discrepancies also stem from the assumptions inherent in the GCE models, particularly in the treatment of nucleosynthesis yields and stellar feedback processes at high metallicities. For instance, we increased the initial mass of gas in the simulation from the default values. While this approach enables us to extend the model to higher $[\text{Fe}/\text{H}]$ values, it somewhat diverges from a truly realistic representation of our Galaxy (see Figure 3a).
- The failure of our models to reproduce the observed Na enhancement relative to iron at super-Solar metallicities implies a potential lack of iron enrichment in these stars. In other words, the younger old thick disc Solar-like stars may have experienced a chemical evolution in which the progenitor ‘pre-stellar’ cloud was under-abundant in pollutants expelled by Type Ia supernovae (e.g., iron).

Among the models examined, the K10WW95 model most closely passes through the observational data until Solar values and then declines from around $[\text{Fe}/\text{H}] \sim 0.1$ dex instead of continuing the observed upturn in the data. In contrast, the K10K06 and K10C22K06 models tend to predict higher $[\text{Na}/\text{Fe}]$ values at all metallicities sampled by the data. A key factor in the $[\text{Na}/\text{Fe}]$ enrichment is the contribution from AGB stars, which produce Na through the Ne-Na cycle during HBB at low metallicity and second dredge-up at higher metallicities (Mowlavi 1999; Ventura et al. 2013; Karakas & Lattanzio 2014). The efficiency of this process increases at higher metallicities due to enhanced neon abundances (Karakas & Lattanzio 2014; Cristallo et al. 2015). We note that the K10C22K06 model displays the most prominent increase in $[\text{Na}/\text{Fe}]$ as a function of $[\text{Fe}/\text{H}]$, though with our current GCE set-up, the overall $[\text{Na}/\text{Fe}]$ values are well below those of the observations (Figure 4, panel c). However, one could envisage a scenario in which SNe Ia played a lesser role in polluting the interstellar gas that gave rise to forming stars in our sample. In such a case, iron would be under-abundant, which would naturally lead to an increase in the absolute abundance of $[\text{Na}/\text{Fe}]$, plausibly bringing the models into better agreement with observations.

Notably, none of our tested models that combine massive and AGB stars and either Chandrasekhar- or sub-Chandrasekhar-mass SNe Ia successfully replicate the observed $[\text{Na}/\text{Fe}]$ upturn at super Solar metallicities (see Figure 4c). As a test, we tried two sets of SN Ia yields from WD mergers: either the two-explosion model as already

discussed, in addition to the single-explosion model of Pakmor et al. (2022) in which only the primary WD explodes. The models show no observable differences in $[\text{Na}/\text{Fe}]$ predictions (Figure 5A1). Collectively, these results suggest that the nature of the SN Ia progenitor does not explain the discrepancy between the models and the observations in metal-rich disc stars in this work. The physical mechanism behind this suppression remains unclear, though potential drivers include delayed chemical mixing in the thick disc or environmental factors altering (suppressing) SNe Ia progenitor evolution. While speculative, this last line of inquiry aligns most closely with observational trends and requires prioritising these in future GCE studies.

5 CONCLUSIONS

In this paper, we have examined Na enrichment in Solar-type Galactic thick disc stars at super Solar metallicities, utilising observational data from the GALAH DR3 survey and testing GCE models that incorporate nucleosynthetic yields from massive stars, AGB stars ($1.0 \leq M_{\odot} \leq 8.0$) and two explosion mechanisms of SNe Ia (Chandrasekhar- and sub-Chandrasekhar mass explosions). At the time of writing, nucleosynthetic yields for sub-Chandrasekhar mass SNe Ia from WD mergers were only available for Solar metallicity and one set of WD merger masses. We acknowledge that future studies should aim to incorporate SN Ia yields at a variety of metallicities (and masses in the case of sub-Chandrasekhar-mass scenarios) once they become more readily available.

Critically, our analysis demonstrates that all four models incorporated in this study fail to replicate the $[\text{Na}/\text{Fe}]$ enrichment at super-Solar metallicities. These findings suggest that our understanding of Na enrichment in metal-rich, thick-disc, Solar-type stars remains insufficient, potentially reflecting gaps in the assumptions underpinning state-of-the-art nucleosynthesis prescriptions. The inability of these models to reproduce the observed trend – despite their calibration with modern stellar physics – implies that key processes, such as metallicity-dependent mass-loss rates in AGB stars, proton-capture reactions efficiencies in CC SNe, or the role of binary interactions.

While the K10WW95 model using WW95 massive stars initially appears promising – in terms of matching the $[\text{Na}/\text{Fe}]$ level up to Solar metallicity (see Figure 2), it too deviates significantly at super Solar regimes (see panel (c) of Figure 4). These findings indicate that attributing the super Solar $[\text{Na}/\text{Fe}]$ upturn primarily to metallicity-dependent CC SNe yields (e.g. Arnould & Norgaard 1978) reveals a challenging puzzle that remains unsolved. In addition, although SNe Ia produce more ^{56}Fe compared to CC SNe, the result of the GCE prediction still fails to correctly replicate the Na enrichment in the Solar-type sample used in this study. The enrichment of Na at super-Solar metallicity caused by the secondary dredge-up effect in AGB star models was unable to account for the observed increase in $[\text{Na}/\text{Fe}]$ in the data, despite including high-Z AGB yields in the K10C22K06 model. As a result, future research should focus on enhancing nucleosynthesis models over various metallicities from all sources to better align theoretical predictions with the observed $[\text{Na}/\text{Fe}]$ trends in the Galactic disc and other stellar populations. In this sense, some discrepancies between GCE models and observational data for a sub-sample of nearby Galactic disc stars might even be expected and can provide valuable insights into the complexities of stellar evolution and chemical enrichment. Specifically, metallicity-dependent SN Ia yields – including sub-Chandrasekhar mergers across the mass and metallicity range should be explored, although we acknowledge that this can be a computationally intensive exercise. However, these systems exhibit isotopic sensitivities,

e.g., α -elements and neutron-rich isotopes [Travaglio et al. \(2005\)](#), but can be explored further.

ACKNOWLEDGEMENTS

This work was supported by the Australian Research Council Centre of Excellence for All-Sky Astrophysics in 3 Dimensions (ASTRO 3D) through project number CE170100013. Part of it was funded through AJR's Australia Research Council Future Fellowship award number FT170100243. EKO, AJR and IRS also acknowledge the support of the Australia-Germany Joint Research Cooperation Scheme (Funding Application ID: 57654415), which facilitated our collaboration with Researchers from the Max Planck Institute for Astronomy in Heidelberg, Germany.

FACILITIES

AAT with 2df-HERMES at Siding Spring Observatory: The GALAH Survey is based on data acquired through the Australian Astronomical Observatory, under programs: A/2013B/13 (The GALAH pilot survey); A/2014A/25, A/2015A/19, A/2017A/18 (The GALAH survey phase 1), A/2018 A/18 (Open clusters with HERMES), A/2019A/1 (Hierarchical star formation in Ori OB1), A/2019A/15 (The GALAH survey phase 2), A/2015B/19, A/2016A/22, A/2016B/10, A/2017B/16, A/2018B/15 (The HERMES-TESS program), and A/2015A/3, A/2015B/1, A/2015B/19, A/2016A/22, A/2016B/12, A/2017A/14, (The HERMES K2-follow-up program). This paper includes data provided by AAO Data Central (data-central.aao.gov.au). **Gaia:** This work has made use of data from the European Space Agency (ESA) mission *Gaia* (<http://www.cosmos.esa.int/gaia>), processed by the *Gaia* Data Processing and Analysis Consortium (DPAC, <http://www.cosmos.esa.int/web/gaia/dpac/consortium>). Funding for the DPAC has been provided by national institutions, particularly the institutions participating in the *Gaia* Multilateral Agreement. **Other facilities:** This publication makes use of data products from the Two Micron All Sky Survey ([Skrutskie et al. 2006](#)) and the CDS VizieR catalogue access tool ([Ochsenbein et al. 2000](#)).

SOFTWARE

The research for this publication was coded in PYTHON (version 3.7.4) and included its packages ASTROPY (v. 3.2.2; [Astropy Collaboration et al. 2013, 2018](#)), CORNER (v. 2.0.1; [Foreman-Mackey 2016](#)), IPYTHON (v. 7.8.0; [Pérez & Granger 2007](#)), MATPLOTLIB (v. 3.1.3; [Hunter 2007](#)), NUMPY (v. 1.17.2; [Walt et al. 2011](#)), SCIPY (version 1.3.1; [Virtanen et al. 2020](#)), We further made use of TOPCAT (version 4.7; [Taylor 2005](#));

DATA AVAILABILITY

The data used for this study is published by [Buder et al. \(2021\)](#) and can be accessed publicly via <https://docs.datacentral.org.au/galah/dr3/overview/>

REFERENCES

- Amarsi A. M., et al., 2020, *A&A*, **642**, A62
- Andrews B. H., Weinberg D. H., Schönrich R., Johnson J. A., 2017, *ApJ*, **835**, 224
- Appenzeller I., 1982, *Fundamentals Cosmic Phys.*, **7**, 313
- Arcones A., Thielemann F.-K., 2023, *A&ARv*, **31**, 1
- Arnett W. D., 1971, *ApJ*, **166**, 153
- Arnett W. D., 1978, *ApJ*, **219**, 1008
- Arnett D., 1996, *Supernovae and Nucleosynthesis: An Investigation of the History of Matter from the Big Bang to the Present*
- Arnould M., Norgaard H., 1978, *A&A*, **64**, 195
- Astropy Collaboration et al., 2013, *A&A*, **558**, A33
- Astropy Collaboration et al., 2018, *AJ*, **156**, 123
- Beccari G., Carraro G., 2015, in Boffin H. M. J., Carraro G., Beccari G., eds, *Astrophysics and Space Science Library Vol. 413, Astrophysics and Space Science Library*. p. 1 ([arXiv:1406.3462](#)), doi:10.1007/978-3-662-44434-4_1
- Bensby T., Feltzing S., Oey M. S., 2014, *A&A*, **562**, A71
- Bensby T., et al., 2017, *A&A*, **605**, A89
- Bovy J., 2015, *ApJS*, **216**, 29
- Bravo E., Isern J., Piersanti L., 2024, *A&A*, **683**, A237
- Buder S., et al., 2021, *MNRAS*, **506**, 150
- Cavichia O., et al., 2024, *MNRAS*, **532**, 2331
- Cayrel de Strobel G., Chauve-Godard J., Hernandez G., Vaziraga M. J., 1970, *A&A*, **7**, 408
- Chiappini C., 2009, in Andersen J., Nordström B., Bland-Hawthorn J., eds, *IAU Symposium Vol. 254, The Galaxy Disk in Cosmological Context*. pp 191–196, doi:10.1017/S1743921308027580
- Cinquegrana G. C., Karakas A. I., 2022, *MNRAS*, **510**, 1557
- Côté B., Ritter C., 2018, OMEGA: One-zone Model for the Evolution of Galaxies, *Astrophysics Source Code Library*, record ascl:1806.018
- Côté B., West C., Heger A., Ritter C., O'Shea B. W., Herwig F., Travaglio C., Bisterzo S., 2016, *MNRAS*, **463**, 3755
- Côté B., O'Shea B. W., Ritter C., Herwig F., Venn K. A., 2017, *ApJ*, **835**, 128
- Côté B., Silvia D. W., O'Shea B. W., Smith B., Wise J. H., 2018, *ApJ*, **859**, 67
- Cristallo S., Straniero O., Piersanti L., Gobrecht D., 2015, *ApJS*, **219**, 40
- Cseh B., et al., 2022, *A&A*, **660**, A128
- Dubay L. O., Johnson J. A., Johnson J. W., 2024, *ApJ*, **973**, 55
- Edvardsson B., Andersen J., Gustafsson B., Lambert D. L., Nissen P. E., Tomkin J., 1993, *A&A*, **275**, 101
- Eitner P., Bergemann M., Hansen C. J., Cescutti G., Seitzzahl I. R., Larsen S., Plez B., 2020, *A&A*, **635**, A38
- Eitner P., Bergemann M., Ruiter A. J., Avril O., Seitzzahl I. R., Gent M. R., Côté B., 2023, *A&A*, **677**, A151
- Fenner Y., Gibson B. K., Limongi M., 2002, *Ap&SS*, **281**, 537
- Fink M., Roepke F., Sim S. A., Kromer M., Seitzzahl I., Ruiter A. J., Hillebrandt W., 2012, in Lattanzio J., Karakas A., Lugaro M., Dracoulis G., eds, *Nuclei in the Cosmos (NIC XII)*. p. 50, doi:10.22323/1.146.0050
- Foreman-Mackey D., 2016, *The Journal of Open Source Software*, **1**, 24
- Francois P., 1986, *A&A*, **165**, 183
- Freeman K., Bland-Hawthorn J., 2002, *ARA&A*, **40**, 487
- Gibson B. K., Fenner Y., Renda A., Kawata D., Lee H.-c., 2003, *Publ. Astron. Soc. Australia*, **20**, 401
- Griffith E. J., Weinberg D. H., Buder S., Johnson J. A., Johnson J. W., Vincenzo F., 2022, *ApJ*, **931**, 23
- Hayden M. R., Recio-Blanco A., de Laverny P., Mikolaitis S., Worley C. C., 2017, *A&A*, **608**, L1
- Howell D. A., 2011, *Nature Communications*, **2**, 350
- Hunter J. D., 2007, *Comput Sci Eng*, **9**, 90
- Iwamoto K., Brachwitz F., Nomoto K., Kishimoto N., Umeda H., Hix W. R., Thielemann F.-K., 1999, *ApJS*, **125**, 439
- Jha S. W., Maguire K., Sullivan M., 2019, *Nature Astronomy*, **3**, 706
- Johnson J. W., et al., 2021, *MNRAS*, **508**, 4484
- Karakas A. I., 2010, *MNRAS*, **403**, 1413
- Karakas A., Lattanzio J. C., 2007, *Publ. Astron. Soc. Australia*, **24**, 103

- Karakas A. I., Lattanzio J. C., 2014, *Publ. Astron. Soc. Australia*, **31**, e030
- Kemp A. J., Karakas A. I., Casey A. R., Côté B., Izzard R. G., Osborn Z., 2024, *A&A*, **689**, A222
- Kennicutt Jr. R. C., 1998, *ARA&A*, **36**, 189
- Kobayashi C., Umeda H., Nomoto K., Tominaga N., Ohkubo T., 2006, *ApJ*, **653**, 1145
- Kobayashi C., Karakas A. I., Umeda H., 2011, *MNRAS*, **414**, 3231
- Kobayashi C., Leung S.-C., Nomoto K., 2020a, *ApJ*, **895**, 138
- Kobayashi C., Karakas A. I., Lugaro M., 2020b, *ApJ*, **900**, 179
- Kobayashi C., et al., 2023, *ApJ*, **943**, L12
- Köppen J., Edmunds M. G., 1999, *MNRAS*, **306**, 317
- Kos J., et al., 2017, *MNRAS*, **464**, 1259
- Kroupa P., 2001, *MNRAS*, **322**, 231
- Krumholz M. R., Dekel A., 2012, *ApJ*, **753**, 16
- Kubryk M., Prantzos N., Athanassoula E., 2015, *A&A*, **580**, A126
- Leung S.-C., Nomoto K., 2017, in Kubono S., Kajino T., Nishimura S., Isobe T., Nagataki S., Shima T., Takeda Y., eds, 14th International Symposium on Nuclei in the Cosmos (NIC2016). p. 020506, doi:10.7566/JPSCP.14.020506
- Li W., Chornock R., Leaman J., Filippenko A. V., Poznanski D., Wang X., Ganeshalingam M., Mannucci F., 2011, *MNRAS*, **412**, 1473
- Limongi M., Chieffi A., 2018, *ApJS*, **237**, 13
- Lodders K., Palme H., Gail H. P., 2009, *Landolt Börnstein*, **4B**, 712
- Maoz D., Mannucci F., Brandt T. D., 2012, *MNRAS*, **426**, 3282
- Maoz D., Hallakoun N., Badenes C., 2018, *MNRAS*, **476**, 2584
- Matteucci F., 2014, *Saas-Fee Advanced Course*, **37**, 145
- Matteucci F., 2023, in *Memorie della Societa Astronomica Italiana*. p. 127, doi:10.36116/MEMSAIT_94N2.2023.127
- Matteucci F., Greggio L., 1986, *A&A*, **154**, 279
- Matteucci F., Spitoni E., Recchi S., Valiante R., 2009, *A&A*, **501**, 531
- McWilliam A., 1997, *ARA&A*, **35**, 503
- McWilliam A., Piro A. L., Badenes C., Bravo E., 2018, *ApJ*, **857**, 97
- Mowlavi N., 1999, *A&A*, **350**, 73
- Nissen P. E., Christensen-Dalsgaard J., Mosumgaard J. R., Silva Aguirre V., Spitoni E., Verma K., 2020, *A&A*, **640**, A81
- Nomoto K., Iwamoto K., Nakasato N., Thielemann F. K., Brachwitz F., Tsujimoto T., Kubo Y., Kishimoto N., 1997, *Nuclear Phys. A*, **621**, 467
- Nomoto K., Kobayashi C., Tominaga N., 2013, *ARA&A*, **51**, 457
- Ochsenbein F., Bauer P., Marcout J., 2000, *A&AS*, **143**, 23
- Owusu E. K., Buder S., Ruiter A. J., Seitzzahl I. R., Rodriguez-Segovia N., 2024, *PASA*, **41**, e092
- Pakmor R., et al., 2022, *MNRAS*, **517**, 5260
- Pérez F., Granger B. E., 2007, *Comput Sci Eng*, **9**, 21
- Ratcliffe B. L., Ness M. K., Buck T., Johnston K. V., Sen B., Beraldo e Silva L., Debattista V. P., 2022, *ApJ*, **924**, 60
- Recio-Blanco A., et al., 2014, *A&A*, **567**, A5
- Ruiter A. J., Seitzzahl I. R., 2025, *A&ARv*, **33**, 1
- Ruiter A. J., Belczynski K., Sim S. A., Hillebrandt W., Fryer C. L., Fink M., Kromer M., 2011, *MNRAS*, **417**, 408
- Rybizki J., Just A., Rix H.-W., 2017, *A&A*, **605**, A59
- Salpeter E. E., 1955, *ApJ*, **121**, 161
- Sánchez Almeida J., Elmegreen B. G., Muñoz-Tuñón C., Elmegreen D. M., 2014, *A&ARv*, **22**, 71
- Schoettler C., Owen J. E., 2024, *MNRAS*, **533**, 3484
- Seitzzahl I. R., et al., 2013a, *MNRAS*, **429**, 1156
- Seitzzahl I. R., Cescutti G., Röpke F. K., Ruiter A. J., Pakmor R., 2013b, *A&A*, **559**, L5
- Sellwood J. A., Binney J. J., 2002, *MNRAS*, **336**, 785
- Shi J. R., Gehren T., Zhao G., 2004, *A&A*, **423**, 683
- Skrutskie M. F., et al., 2006, *AJ*, **131**, 1163
- Steinhardt C. L., Rusakov V., Clark T. H., Diaconu A., Forbes J., McPartland C., Sneppen A., Weaver J., 2023, *ApJ*, **949**, L38
- Takeda Y., Takada-Hidai M., 1994, *PASJ*, **46**, 395
- Taylor M. B., 2005, in Shopbell P., Britton M., Ebert R., eds, *ASPC Vol. 347, Astronomical Data Analysis Software and Systems XIV*. p. 29
- Timmer F. X., Woosley S. E., Weaver T. A., 1995, *ApJS*, **98**, 617
- Tinsley B. M., Larson R. B., 1978, *ApJ*, **221**, 554
- Travaglio C., Hillebrandt W., Reinecke M., 2005, *A&A*, **443**, 1007
- Tsujimoto T., Nomoto K., Yoshii Y., Hashimoto M., Yanagida S., Thielemann F. K., 1995, *MNRAS*, **277**, 945
- Ventura P., Di Criscienzo M., Carini R., D'Antona F., 2013, *MNRAS*, **431**, 3642
- Vink J. S., 2018, *A&A*, **615**, A119
- Virtanen P., et al., 2020, *Nature Methods*, **17**, 261
- Walt S. v. d., Colbert S. C., Varoquaux G., 2011, *Comput Sci Eng*, **13**, 22
- Wheeler J. C., Sneden C., Truran J. J. W., 1989, *ARA&A*, **27**, 279
- Woosley S. E., Weaver T. A., 1995, *ApJS*, **101**, 181
- Zahid H. J., Dima G. I., Kudritzki R.-P., Kewley L. J., Geller M. J., Hwang H. S., Silverman J. D., Kashino D., 2014, *ApJ*, **791**, 130
- den Hartogh J. W., et al., 2023, *A&A*, **672**, A143
- van den Hoek L. B., Groenewegen M. A. T., 1997, *A&AS*, **123**, 305

APPENDIX A: EXPLORING THE EFFECT OF SUB-CHANDRASEKHAR SN IA

This paper has been typeset from a \LaTeX file prepared by the author.

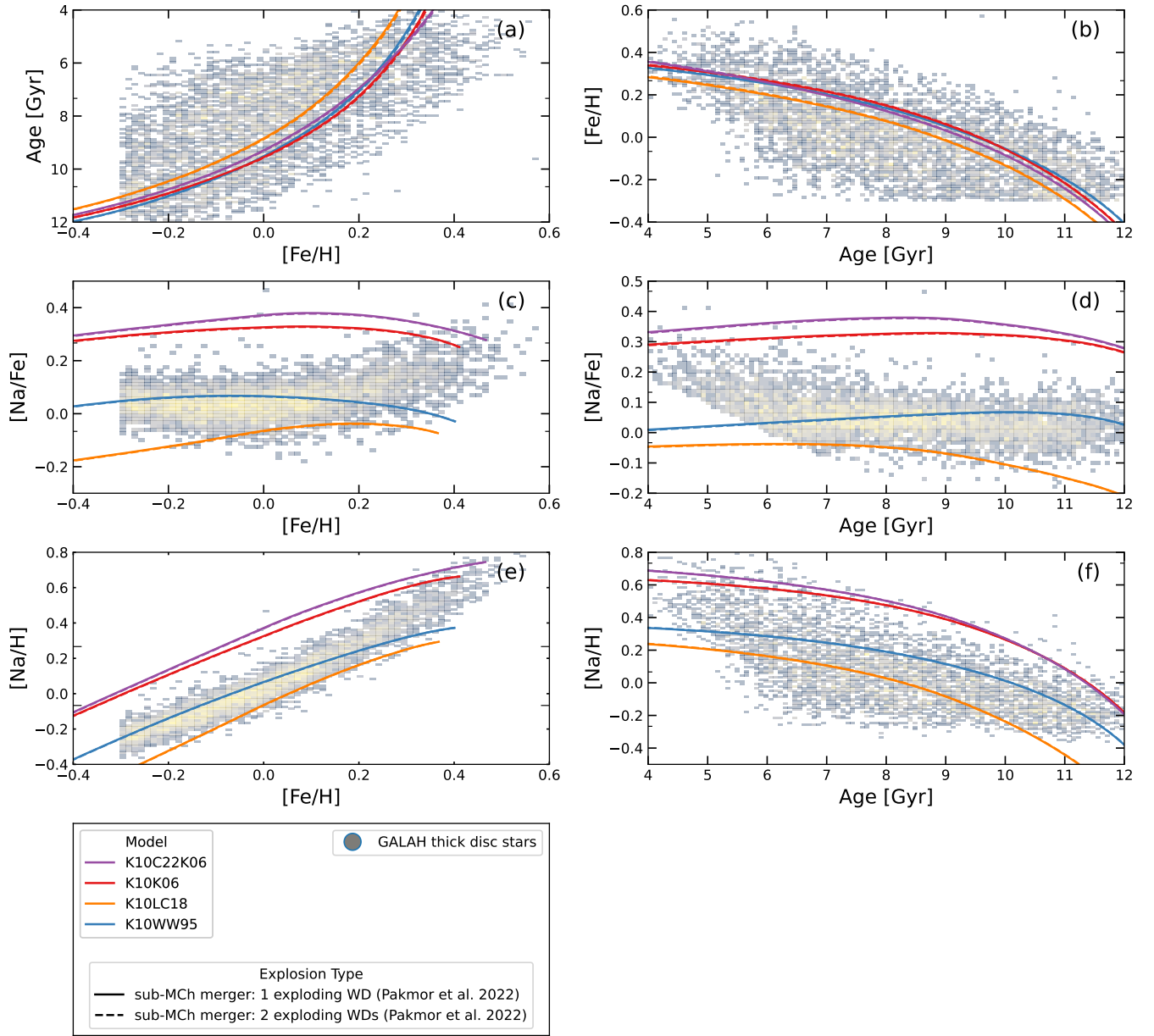


Figure A1. Na abundance relation for different parameters [Na/Fe], Age, [Fe/H] planes. We used the [Pakmor et al. \(2022\)](#) SNe Ia sub-Chandrasekhar (1 and 2 explosion). For the GALAH data, yellow regions reflect a higher number density of stars.